Journal of Materials Chemistry A

PAPER

Cite this: J. Mater. Chem. A, 2018, 6, 20852

Dynamical stabilization in delafossite nitrides for solar energy conversion†

N. J. Szymanski, [a] L. N. Walters, [b] O. Hellman, [ce] D. Gall [d] and S. V. Khare*[a]

Delafossite structured ternary nitrides, ABN_2, have been of recent experimental investigation for applications such as tandem solar and photoelectrochemical cells. We present a thorough first principles computational investigation of their stability, electronic structure, and optical properties. Nine compounds, where A = Cu, Ag, Au and B = V, Nb, Ta, were studied. For three of these compounds, $CuTaN_2$, $CuNbN_2$, and $AgTaN_2$, our computations agree well with experimental results. Optimized lattice parameters, formation energies, and mechanical properties have been computed using the generalized gradient approximation (GGA). Phonon density of states computed at zero-temperature shows that all compounds are dynamically unstable at low temperatures. Including finite-temperature anharmonic effects stabilizes all compounds at 300 K, with the exception of $AgVN_2$. Analysis of Crystal Orbital Hamiltonian Populations (COHP) provides insight into the bonding and antibonding characters of A–N and B–N pairs. Instability at low temperatures can be attributed to strong A–N antibonding character near the Fermi energy. B–N bonding is found to be crucial in maintaining stability of the structure. $AgVN_2$ is the only compound to display significant B–N antibonding below the Fermi energy, as well as the strongest degree of A–N antibonding, both of which provide explanation for the sustained instability of this compound up to 900 K. Hybrid functional calculations of electronic and optical properties show that real static dielectric constants in the semiconductors are related to corresponding band gaps through the Moss relation. $CuTaN_2$, $CuNbN_2$, $AgTaN_2$, $AgNbN_2$, $AgVN_2$, $AuTaN_2$, and $AuNbN_2$ exhibit indirect electronic band gaps while $CuVN_2$ and $AuVN_2$ are metallic. Imaginary parts of the dielectric function are characterized by d–d interband transitions in the semiconductors and d–d intraband transitions in the metals. Four compounds, $CuTaN_2$, $CuNbN_2$, $AgTaN_2$, and $AgNbN_2$, are predicted to exhibit large light absorption in the range of 1.0 to 1.7 eV, therefore making these materials good candidates for solar-energy conversion applications. Two compounds, $AuTaN_2$ and $AuNbN_2$, have band gaps and absorption onsets near the ideal range for obtaining high solar-cell conversion efficiency, suggesting that these compounds could become potential candidates as absorber materials in tandem solar cells or for band-gap engineering by alloying.

Received 3rd August 2018
Accepted 28th September 2018

DOI: 10.1039/c8ta07536k

rsc.li/materials-a

1 Introduction

The pursuit of new materials, beyond silicon, in solar cell applications has given rise to research in many different material classes.[1,2] Material families including cadmium telluride,[3] copper indium diselenide,[4] perovskites,[5] organic materials,[6] and oxides[7,8] have been most widely studied. However, nitrides have recently started to receive more interest. Numerous binary nitrides have been studied extensively, and have been found to display potentially advantageous mechanical,[9] electronic,[10,11] and optical properties.[12] In contrast, ternary nitrides remain relatively unexplored, with early findings indicating that they could also provide beneficial features.[13–15] One particularly interesting system of ternary nitrides is that which exhibits the delafossite structure.

Thus far, three delafossite nitrides have been synthesized experimentally. The first to be discovered was $CuTaN_2$, the structure of which was reported in 1991.[16] However, the properties of this compound were unknown until recently. In 2013, a study reported the energetic, electronic, and optical properties of $CuTaN_2$.[15] Both experimental and theoretical results indicated that the material exhibited a band gap of approximately

[a]Department of Physics and Astronomy, University of Toledo, Toledo, OH 43606, USA. E-mail: sanjay.khare@utoledo.edu

[b]Department of Materials Science and Engineering, Northwestern University, Illinois 60208, USA

[c]Department of Applied Physics and Material Science, California Institute of Technology, Pasadena, CA 91125, USA

[d]Department of Materials Science and Engineering, Rensselaer Polytechnic Institute, Troy, NY 12180, USA

[e]Department of Physics, Chemistry, and Biology (IFM), Linköping University, SE-581 83, Linköping, Sweden

† Electronic supplementary information (ESI) available. See DOI: 10.1039/c8ta07536k

1.3 eV and a significantly large absorption in the range of 1.4–1.5 eV. The next delafossite nitride to be discovered was $AgTaN_2$, which was first synthesized and studied in 2011.[17] A band gap of 1.65 eV and an absorption onset near 2.0 eV was reported. Lastly, $CuNbN_2$ was discovered in 2013.[14] The compound was found to have a band gap of 0.9 eV and an absorption onset of 1.3 eV. These results indicate that each of the delafossite nitride has high potential for application in solar cells.

Given the interesting properties of these nitrides, it would be beneficial to expand the number of available compounds for band gap tuning by doping or alloying in applications such as tandem solar cells or other related applications. Therefore, we have studied the structural, thermodynamic, energetic, elastic, electronic, and optical properties of nine ternary nitrides with an underlying delafossite geometry. The compounds in focus are of the form ABN_2, where A represents group 11 transition metals (Cu, Ag, and Au), and B represents group 5 transition metals (V, Nb, and Ta). A elements were chosen based on their d^{10} configurations, which are expected to overlap with the 2p electrons of the N ions to form strong covalent bonds. B elements were chosen based on their relatively low electronegativity and likelihood to form strong ionic bonds with N. These two characteristics are crucial to maintain the delafossite structure.[18] We have implemented first principles methods to study the stability of these materials, as well as their electronic and optical properties. By doing so, we have identified several delafossite nitrides which are promising for usage in solar cell applications.

2 Computational methods

All density functional theory (DFT) calculations have been implemented using the Vienna Ab Initio Simulation Package (VASP).[19–22] We have utilized the Perdew–Burke–Ernzerhof (PBE) generalized gradient approximation exchange correlation functional and the projector augmented wave method.[23,24] A plane wave cutoff energy of 520 eV was used for the plane-wave basis set. The Ta_pv potential, in which semi-core p electrons are treated as valence states, was chosen for tantalum, while the Nb_sv and V_sv potentials, in which the semi-core s and p electrons are treated as valence states, were chosen for niobium and vanadium. The default potentials were used for copper, silver, gold, and nitrogen. All *k*-point meshes consisted of 4000 *k*-points per reciprocal atom (KPPRA). A convergence criterion of 10^{-6} eV per atom with a Gaussian smearing value of width 0.05 eV was chosen for the electronic minimizations.

Experimental structures were obtained from the literature for $CuTaN_2$,[16] $CuNbN_2$,[14] and $AgTaN_2$.[17] These were then geometrically optimized, allowing the unit cell shape, volume, and ionic positions to be relaxed until forces acting on each atom were less than or equal to 0.01 eV $Å^{-1}$. The remaining six compounds in this study ($CuVN_2$, $AgNbN_2$, $AgVN_2$, $AuTaN_2$, $AuNbN_2$, and $AuVN_2$) have not been experimentally synthesized, and thus no structural data was available. Therefore, we constructed a unit cell with dimensions and ionic positions equal to that of the known delafossite nitrides and used this as a starting point for the relaxations. Optimization was performed until convergence was obtained, in the same manner as previously described.

Once the relaxed structures were obtained, high-precision static calculations were performed in order to obtain an accurate final energy. These energies were then used to calculate the formation energy of each material. The formation energy can be defined as the difference between the energy of the compound and the energies of its constituents in their ground states. Accordingly, the following equation was used:

$$\Delta E_{\text{form}} = [E(ABN_2) - E(A) - E(B) - E(N_2)]/4 \quad (1)$$

where A = (Cu, Ag, or Au) and B = (Ta, Nb, or V). Energies were also computed with respect to their respective ternary A-B-N convex hulls. All known stable binaries, taken from Materials Project,[25] were considered.

To determine elastic constants, we have implemented density functional perturbation theory to compute the Hessian matrix for each compound.[26] This matrix contains the second derivatives of energy with respect to the atomic positions of the system. By analyzing these values, we obtained the elastic tensor of each compound. Since all materials in this study exhibit hexagonal geometry, the relevant values are C_{11}, C_{12}, C_{13}, C_{33}, C_{44}, and C_{66}.[27] The elastic constants have been used to compute the Voigt averages of bulk (K_V) and shear (G_V) modulus, which are defined as the following:[28]

$$K_V = [2(C_{11} + C_{12}) + 4C_{13} + C_{33}]/9 \quad (2)$$

$$G_V = [C_{11} + C_{12} + 2C_{33} - 4C_{13} + 12(C_{44} + C_{66})]/30 \quad (3)$$

These were then used to compute Pugh's ratio ($k = G_V/K_V$) and Vickers hardness (H_v), as given by Tian *et al.*:[29]

$$H_v = 0.92k^{1.137}G^{0.708} \quad (4)$$

To investigate dynamical stability of these delafossite compounds, we have computed phonon dispersion curves using two distinct methods: (i) the quasiharmonic approximation (QHA)[30] and (ii) the temperature dependent effective potential method (TDEP).[31,32] QHA assumes anharmonic effects are insignificant and employs zero-temperature DFT methods to compute phonon frequencies. In this work, we calculated the Hessian matrix of each compound on a 4 × 4 × 2 supercell using density functional perturbation theory (DFPT).[19–22] Utilizing these results along with the PHONOPY code,[33] quasiharmonic phonon frequencies were calculated. Although QHA works well for many classes of materials,[33,34] it fails when applied to compounds which are dynamically unstable at zero-temperature.[30–32] Therefore, we have also implemented the recently-developed TDEP method, which is able to accurately describe finite-temperature lattice dynamics. This method accounts for anharmonic effects by constructing interatomic force-constant matrices using information obtained from molecular dynamics trajectories.[31,32] In this work, Born-Oppenheimer molecular dynamics were conducted on 4 × 4 × 2 supercells of the conventional 12-atom unit cells using canonical NVT ensembles at a temperature of 300 K, controlled

by a Nosé thermostat.[35] Simulations were performed for 8000 time steps of 2 fs each. Using the results of these runs, interatomic forces and resulting phonon frequencies were calculated with the TDEP package.[31,32]

The Heyd-Scuseria-Ernzerhof hybrid functional (HSE06)[36] was employed to study electronic and optical properties. Hybrid functionals incorporate a portion of exact exchange from Hartree–Fock theory, mixed with exchange from standard DFT methods. For the HSE06 functional, 25% of the Hartree–Fock exact exchange is used, while the remaining 75% is from GGA. For all computations implementing hybrid functionals, a 24 × 24 × 6 k-point mesh was used to evaluate the GGA portion, while the Hartree–Fock portion was evaluated on a smaller 8 × 8 × 2 grid. Using this method, on-site electronic densities were calculated, allowing us to plot the local density of states. We have also computed the complex dielectric function $(\varepsilon_1 + i\varepsilon_2)$[37,38] as a function of photon energy $(\hbar\omega)$ for each material. From these values, extinction coefficients $\kappa(\omega)$ and absorption coefficients $\alpha(\omega)$ were calculated using the following equations:[39]

$$\alpha(\omega) = 2\omega\kappa(\omega)/c \text{ where } \kappa(\omega) = [((\varepsilon_1{}^2 + \varepsilon_2{}^2)^{1/2} - \varepsilon_1)/2]^{1/2} \quad (5)$$

3 Results and discussion

3.1 Structural, mechanical, and vibrational properties

There are two known types of delafossite structures: the 3R polytype and the 2H polytype. Previous experimental works show $CuTaN_2$, $CuNbN_2$, and $AgTaN_2$ exhibit the 3R type structure, which has a space group symmetry of $R\bar{3}m$.[14,16,17] We find that after full geometric optimization, $CuVN_2$, $AgNbN_2$, $AgVN_2$, $AuTaN_2$, $AuNbN_2$, and $AuVN_2$ also maintain the 3R polytype. The general unit cell for a 3R type delafossite-structured ABN_2 compound is displayed in Fig. 1. The structure can be visualized as consisting of two layers: one which consists of BN_6 octahedra, and one in which A atoms are linearly coordinated to the N atoms of the octahedra.[15] B–N octahedra are known to display significant angular distortions due to A–N interactions, as well as electrostatic repulsion between nearest B ions.[18] A atoms exhibit hexagonal bipyramidal coordination consisting of short A–N axial bonds and long A–A equatorial bonds.

Optimized lattice parameters are displayed in Table 1. The delafossite structure, being hexagonal, exhibits only two unique lattice constants: a and c. For the nitrides in this work, a ranges from about 2.92 Å to 3.16 Å, and c ranges from about 17.5 Å to 19.0 Å. Our calculated values match well with the experimental data which is available for $CuTaN_2$,[16] $CuNbN_2$,[14] and $AgTaN_2$.[17] Our results do show a very slight over-estimation of the cell size, which is consistent with previous theoretical findings for delafossites[14,15,17] and many other material systems when using GGA.[40] The in-plane lattice constant a is shown to be directly related to ionic radius of the B ion,[41] with a being the smallest for B = V and the largest for B = Ta. In contrast, the out-of-plane lattice constant c is directly related to the atomic radius of the A atom, with c being largest for Ag and smallest for Cu. Au retains a smaller c than Ag due to the well-known lanthanide contraction effect which occurs due to its filled f shells.[42] This effect is clearly visible in the A–N bond lengths. The average Ag–N bond length is 2.14 Å, much larger than the Au–N and Cu–N bond lengths of 2.06 Å and 1.85 Å respectively. We find that angular distortion of the B–N octahedra also varies for each compound. The degree of distortion, which can be quantified by the standard deviation in bond angles, appears to be directly related to the size of the A and B atoms. These standard deviations are listed in Table S1 of the ESI.† The data indicates that compounds containing Ag display the strongest degree of angular distortion, being related to the large radius of Ag. Internal atomic parameters are also listed in Table S2.†

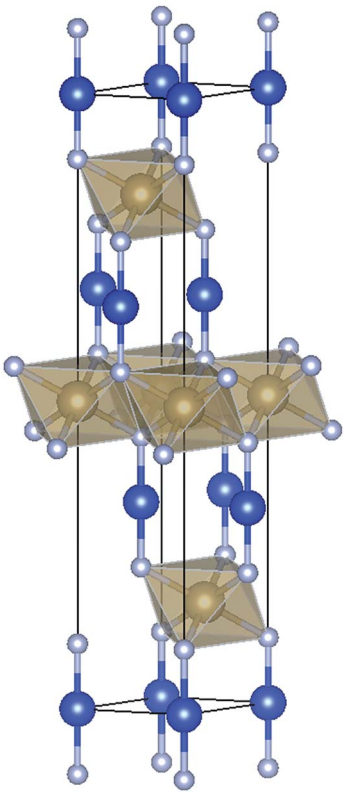

Fig. 1 The delafossite structured unit cell, of the form ABN_2. The large dark blue spheres represent A atoms, the large tan spheres represent B atoms, and the small light blue spheres represent N atoms. This visualization was obtained through use of VESTA.[69]

The calculated formation energies can be found in Table 2. Our findings indicate that all compounds provide an energetically favorable configuration as opposed to the constituent elements in their ground states, which agrees with previous reports for $CuTaN_2$, $CuNbN_2$, and $AgTaN_2$.[14,15] We find that the formation energy values range from −0.16 to −0.55 eV per atom, with $CuTaN_2$ being the most energetically stable material. The results show that for ABN_2, B = Ta causes the most energetically favorable compounds, whereas B = V results in the least energetically favorable compounds. Thus, increasing the number of filled electronic shells (moving down the column in the periodic table) in the B element leads to a more stable compound. Energies with respect to ternary convex hulls (shown in Fig. S1 of the ESI†) are also listed in Table 2. We find that all ABN_2 compounds lie slightly above the hull by amounts

Table 1 Structural parameters for the unit cell of each compound. Calculated lattice constants, a and c, and volume, V, are shown. For comparison, experimentally measured parameters are listed in parentheses

Compound	a (Å)	c (Å)	c/a	V (Å^3)
$CuTaN_2$	3.156 (3.136)[a]	17.565 (17.438)[a]	5.565 (5.561)[a]	151.532 (148.5)[a]
$CuNbN_2$	3.152 (3.142)[b]	17.518 (17.385)[b]	5.444 (5.533)[b]	150.740 (148.67)[b]
$CuVN_2$	2.895	17.520	6.052	127.138
$AgTaN_2$	3.159 (3.141)[c]	18.999 (18.81)[c]	6.014 (5.989)[c]	164.147 (160.7)[c]
$AgNbN_2$	3.154	18.946	6.007	163.252
$AgVN_2$	2.917	18.932	6.490	139.527
$AuTaN_2$	3.164	18.806	5.944	163.041
$AuNbN_2$	3.161	18.746	5.930	162.228
$AuVN_2$	2.921	18.768	6.394	138.663

[a] Ref. [15]. [b] Ref. [14]. [c] Ref. [17].

Table 2 Formation energy with respect to constituents in their elemental ground states and energy with respect to the ternary A-B-N convex hull of each compound, computed through implementation of standard GGA

Compound	Formation energy (eV per atom)	Energy above hull (eV per atom)
$CuTaN_2$	−0.55	0.06
$CuNbN_2$	−0.46	0.13
$CuVN_2$	−0.29	0.29
$AgTaN_2$	−0.47	0.09
$AgNbN_2$	−0.37	0.15
$AgVN_2$	−0.16	0.30
$AuTaN_2$	−0.45	0.25
$AuNbN_2$	−0.36	0.27
$AuVN_2$	−0.20	0.18

ranging from 0.06 to 0.30 eV per atom, with $AgVN_2$ being the least energetically favorable composition. This agrees with previous results for known delafossite nitrides.[15] Despite these compounds only being thermodynamically metastable, experimental findings have shown that the known delafossite nitrides ($CuTaN_2$, $CuNbN_2$, and $AgTaN_2$) do not decompose at ambient conditions, indicating relative stability.[14–17]

Computed elastic properties are displayed in Table 3. We find K_V values in the range of 173 to 215 GPa and G_V values in the range of 81 to 97 GPa. We find consistent trends in these properties depending on the given elements A and B within ABN_2. B = Nb results in lower bulk and shear moduli, whereas B = V causes a high bulk and shear moduli. A = Ag leads to the lowest bulk and shear moduli, whereas A = Cu or Au both cause high bulk and shear moduli. These results coincide closely with the underlying structures, as volume appears to be inversely related to bulk moduli, consistent with previous findings.[43–48] Elastic constants can be analyzed to determine whether each compound is mechanically stable. Mouhat and Coudert describe the necessary and sufficient conditions for a compound with hexagonal geometry to be elastically stable.[26] We have checked our values with these conditions, and have found that all materials in this study meet the requirements for elastic stability. The mechanical properties here match closely with similar hexagonal-structured transition metal nitrides.[49,50] The data also indicates that C_{44} directly correlates with K_V which leads to a direct relationship of bulk and shear moduli. Hence, Pugh's ratio remains relatively constant for all compounds, exhibiting values from 0.43 to 0.48, implying ductile nature. Vickers hardness also remains relatively constant, ranging from 6.67 to 7.93 GPa. These values of hardness and ductility are similar to those of currently-used silicon films, indicating delafossites have suitable mechanical properties for solar cell applications.[51]

Table 3 Elastic constants (C_{xy}), bulk modulus (K_V), shear modulus (G_V), and Vickers hardness (H_v) for each compound, in units of GPa, and also Pugh's ratio (k). All materials exhibit hexagonal geometry, and therefore six components of the elastic tensor are relevant: C_{11}, C_{12}, C_{13}, C_{33}, C_{44}, and C_{66}

Compound	C_{11}	C_{12}	C_{13}	C_{33}	C_{44}	C_{66}	K_V	G_V	k	H_v
$CuTaN_2$	355	91	123	470	17	132	206	89	0.43	7.00
$CuNbN_2$	340	87	119	464	16	126	199	86	0.43	6.87
$CuVN_2$	333	88	122	565	22	123	210	93	0.44	7.49
$AgTaN_2$	340	85	93	382	16	127	178	85	0.47	7.70
$AgNbN_2$	325	83	91	378	15	121	173	81	0.47	7.31
$AgVN_2$	329	92	91	413	24	119	180	87	0.47	7.93
$AuTaN_2$	349	84	128	474	31	132	206	94	0.48	7.85
$AuNbN_2$	321	93	127	466	29	114	200	85	0.43	6.67
$AuVN_2$	328	116	127	541	51	106	215	97	0.45	7.84

Phonon density of states, computed using both QHA and TDEP, are shown in Fig. 2 and S2 of the ESI.† Interestingly, zero-temperature QHA calculations predict all compounds to contain negative (imaginary) phonon frequencies, indicating dynamical instability, similar to what has been reported for group 5 and 6 transition metal nitrides.[52] However, $CuTaN_2$, $CuNbN_2$, and $AgTaN_2$ have each been synthesized experimentally and are stable in ambient conditions.[14–17] Therefore, we predict these compounds to be stabilized by finite-temperature anharmonic effects. This is a reasonable assumption, as previous experimental studies have shown delafossite-structured ternary oxides to display exceptionally strong anharmonic phonon–phonon coupling which leads to substantial shifts in phonon frequencies.[53–55] Since the mass of nitrogen is less than that of oxygen, it is even more likely that anharmonic contributions are significant, as lighter atoms have

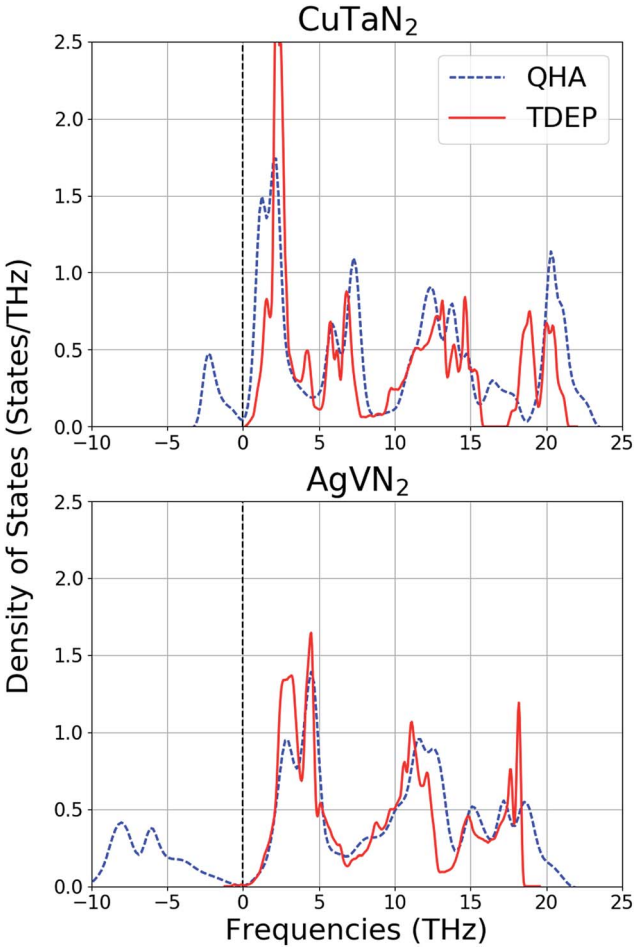

Fig. 2 Phonon density of states for $CuTaN_2$ and $AgVN_2$, calculated using two unique methods: (i) QHA at 0 K and (ii) TDEP at 300 K. Densities are normalized per unit cell. The dashed vertical line represents zero frequency, separating positive (real) from negative (imaginary) frequencies.

larger vibrational amplitudes. Our phonon density of states, computed by TDEP, confirm this prediction: all compounds, except for $AgVN_2$, exhibit purely positive (real) phonon frequencies at 300 K, indicating dynamical stability. Besides the disappearance of all imaginary states at imaginary frequencies, the features of the phonon densities remain very similar to those obtained using QHA at zero-temperature, which are characterized by relatively sharp peaks indicating high acoustic phonon densities below 8 THz and broader less-pronounced peaks around 12–18 THz due to optical phonon modes. For $AgVN_2$, higher temperatures were investigated, and we find that this compound remains unstable up to at least 900 K.

Radial distribution functions, which illustrate variation in bond lengths, are displayed in Fig. S3 of the ESI.† B–N bond lengths are shown to deviate substantially from their equilibrium values, indicating strong distortions of the octahedral complexes as thermal effects are increased. In contrast, A–N bonds remain much closer to their equilibrium lengths and therefore have smaller vibrational amplitudes, likely due to their large atomic masses. To quantify these findings, full widths at half maximum (FWHM) values of A–N and B–N pair distributions are listed in Table S3.† Compounds containing Ag display the largest FWHM values for the A–N distributions, while compounds containing V display the largest values for the B–N distributions. Hence, $AgVN_2$ represents a clear maximum in the data, exhibiting large vibrational amplitudes for both Ag and V, likely reflecting the sustained dynamical instability of this compound at high temperatures.

3.2 Electronic properties

The electronic density of states for each compound is displayed in Fig. S4 of the ESI.† We find that for ABN_2, the clear majority of A (Cu, Ag, and Au) states are occupied, *i.e.*, lie below the Fermi energy. In contrast, the B (Ta, Nb, and V) states are mostly unoccupied, *i.e.*, lie above the Fermi energy, which can be attributed to the strong ionic character of the B–N bonds. N states are found both above and below the Fermi energy, with a majority below. These features agree with previous findings.[14,15,17]

The electronic band gap and band structure of each material can be found in Table 4 and Fig. S5 of the ESI† respectively. Our values match very well with both experimental data and previously calculated values for $CuTaN_2$, $CuNbN_2$, and $AgTaN_2$ as also listed in Table 4.[14,15,17] We find that two of the compounds, $CuVN_2$ and $AuVN_2$, are predicted to be metallic. $AgVN_2$, $AuTaN_2$, and $AuNbN_2$ are shown to be narrow-gap semiconductors, each with band gaps less than 0.7 eV. The remaining four compounds, $CuTaN_2$, $CuNbN_2$, $AgTaN_2$, and $AgNbN_2$, are found to have band gaps within the range of 1.0 to 1.7 eV. All band gaps are indirect (Z–L); however, the lowest conduction band at Z is only very slightly higher in energy than the indirect gap. According to Shockley and Queisser, solar energy conversion with greater than 30% efficiency is possible for semiconductors with band gaps of 0.8–1.7 eV.[56] Therefore, based solely on their electronic properties, $CuTaN_2$, $CuNbN_2$, $AgTaN_2$, and $AgNbN_2$ are potential candidates for solar cell applications. This conclusion agrees with previous reports for $CuTaN_2$, $CuNbN_2$, and $AgTaN_2$,[14,15,17] while $AgNbN_2$ is a prediction from our work.

Table 4 Computed electronic band gap and absorption onset energies, defined as the point at which the absorption coefficient reaches 10^3 cm^{-1}, are shown. All band gaps are indirect. For comparison, experimentally measured values are listed in parentheses

Compound	Band gap (eV)	Absorption onset (eV)
$CuTaN_2$	1.38 (1.3)[a]	1.48 (1.4)[a]
$CuNbN_2$	1.05	1.25 (1.3)[c]
$CuVN_2$	0.00	0.20
$AgTaN_2$	1.62 (1.65)[b]	1.75 (2.0)[b]
$AgNbN_2$	1.48	1.53
$AgVN_2$	0.28	0.44
$AuTaN_2$	0.69	0.88
$AuNbN_2$	0.57	0.65
$AuVN_2$	0.00	0.20

[a] Ref. [15]. [b] Ref. [17]. [c] Ref. [14].

Further analysis of the electron densities shows strong hybridization of the N p states and the metal d states, indicating covalent bonding. Most hybridization occurs at lower energies, generally between −10 to −5 eV. Additionally, although a much greater number of A states are occupied, the B states display stronger hybridization with the N states throughout a wide range of energies, implying that B atoms play a crucial role in the chemical bonding. To provide greater insight into these observations, we have calculated the Crystal Orbital Hamiltonian Populations (COHP) using the LOBSTER package,[57–61] which will allow us to explicitly characterize the bonding and antibonding character of the electron densities. As we are only interested in the occupied bonding states, we have implemented standard GGA (without hybrid functionals), which is known to accurately describe ground state properties. COHP results are shown in Fig. 3 and S6 of the ESI.† For the majority of ABN_2 compounds, we find that the A–N covalent interaction results in strong bonding states at lower energies (−10 to −3 eV) and relatively weaker antibonding states at higher energies (−3 to 0 eV). In contrast, the B–N interactions consist completely of bonding states at all energies below the Fermi energy for almost all compounds, therefore implying the importance of the B element in maintaining stability of structure. Above the Fermi energy, all states are antibonding. Our features agree with previously computed values for $AgTaN_2$.[17] The instability of these compounds at 0 K, as shown by QHA results in Fig. 2 and S1,† can be attributed to the strong A–N antibonding character below the Fermi energy, which is compensated for by anharmonic phonon–phonon interactions at finite temperatures. Fig. 3 reveals $AgVN_2$ to be the only compound for which B–N displays significant antibonding character below the Fermi energy. It also displays the greatest degree of A–N antibonding and nonbonding. The nonbonding is signified by near-zero COHP in Fig. 3 at −4 eV where there is high electronic occupation in the density of states shown in Fig. S4.† These features provide explanation as to why $AgVN_2$ is the only compound in this work to remain unstable at 300 K.

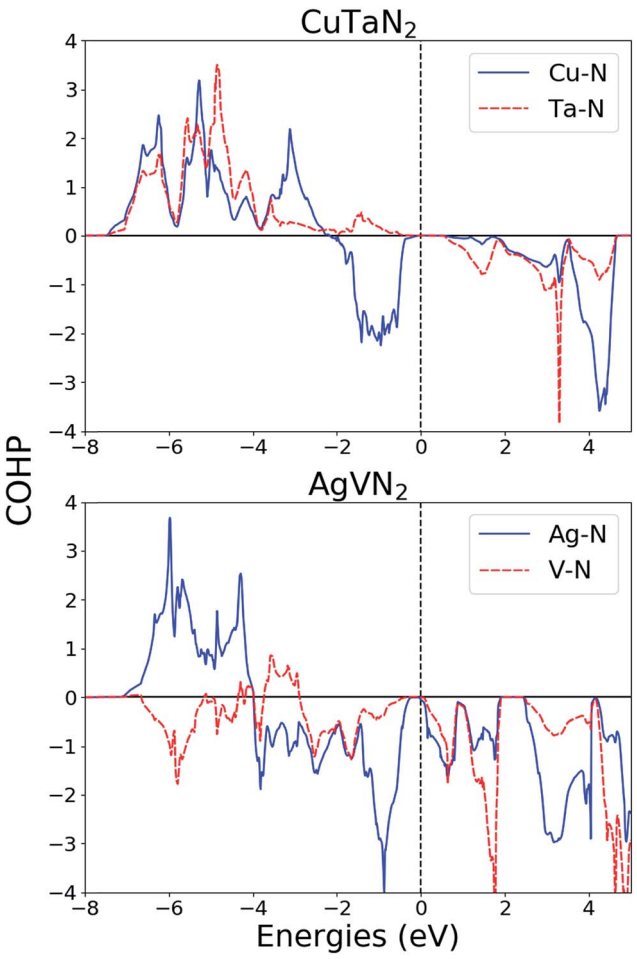

Fig. 3 Crystal Orbital Hamiltonian Populations (COHP) for $CuTaN_2$ and $AgVN_2$, separated into the two major bonding pairs: A–N and B–N. Other A–B and N–N populations are not shown here, as their magnitudes are insignificant compared to the A–N and B–N populations. Bonding states are assigned positive values while antibonding states are assigned negative values. The Fermi energy is set to 0 eV.

The high nonbonding and antibonding character of $AgVN_2$ may be further understood by evaluating the bonding of A and B centered polyhedra.[62] As discussed in section 3.1, B = V leads to the smallest in-plane lattice constant a and therefore the shortest A–A bond lengths. Considering the large radius of Ag, overlap of the A orbitals is strongest in $AgVN_2$, which decreases splitting of σ1g, e2g, and e1g orbitals.[63] Additionally, A = Ag causes the greatest bond angle variance in the B–N octahedra, as shown in Table S1.† Distortions affect the energy of octahedral bonding most when B = V, as its d orbitals are less diffuse than in the 4d and 5d elements. The small orbital splitting energy of V further decreases the Δ_0 energy difference between the e_g and t_{2g} in the octahedra as compared to Nb and Ta.[64,65] As the total d orbital splitting energies in both Ag and V are lessened by these distortions, the nonbonding and antibonding orbitals become more energetically accessible. V also displays the highest electronegativity of the B elements, leading to increased localization of d electrons and enhanced occupation of nonbonding and antibonding orbitals.[66] The combination of all these effects is what causes the strong antibonding character that is displayed in the COHP, resulting in the sustained instability of $AgVN_2$ at higher temperatures. Of the nine compounds in this work, $AuVN_2$ exhibits structural properties most similar to $AgVN_2$. However, the differences in bond lengths and angular distortions are still significant, as discussed in section 3.1 and displayed in Table S1.† These differences are reflected in Fig. S6,† which shows that $AuVN_2$ does not achieve nearly the same degree of antibonding as $AgVN_2$, especially for the V–N bonds.

To investigate thermal effects on bonding characteristics, we have sampled the most stable structure, $CuTaN_2$, at three times (5 ps, 10 ps, and 15 ps) during molecular dynamics calculations at 300 K and re-calculated COHP curves for each. Results are displayed in Fig. S7 of the ESI.† Although minor deviations from the results at 0 K do occur, the data indicates that the major bonding and antibonding features for both A–N and B–N pairs remain relatively constant, implying that our zero-temperature analysis remains unchanged at higher temperatures. Therefore, dynamical stabilization does not occur as a result of

increased bonding character, but instead can be directly attributed to phonon–phonon interactions.

3.3 Optical properties

The complex dielectric functions are displayed in Fig. S8 of the ESI.† Due to the hexagonal structure of the compounds, the optical properties are anisotropic. Therefore, we have plotted both ε_1 and ε_2 in their directional components. Compounds containing Ta and Nb are characterized by relatively low static dielectric constants (ε_1 in the range of 5 to 15 at low energies), while compounds containing V exhibit much higher values (ε_1 in the range of 20 to 40 at low energies). We find that the dielectric constants of all non-metallic compounds in this work are related to their corresponding electronic band gap energies through the Moss relation, which states that the refractive index of a semiconductor is related to its band gap as follows: $n^4 E_g = 95$ eV.[67] Since $n = \sqrt{\varepsilon_r}$ for non-magnetic materials, we can rearrange the equation to obtain $\varepsilon_r = \sqrt{95\ \text{eV}/E_g}$. In Fig. 4, we have plotted our computed static dielectric constants *vs.* electronic band gaps for all non-metallic compounds in this work, as well as the curve corresponding to the ideal Moss relation. We find that all semiconductors correlate very closely to the Moss relation. The imaginary portion of the dielectric function, ε_2, remains zero-valued below the band gap for the semiconductors, and rises substantially at energies immediately above the gap. From Fig. S4,† we conclude that this rise in ε_2 is mainly attributed to d–d interband transitions between the occupied A (Cu, Ag, Au) states and the unoccupied B (Ta, Nb, V) states. In the metallic compounds ($CuVN_2$ and $AuVN_2$), ε_2 rises substantially at low energies, which is mainly attributed to intraband transitions within the d states of V near the Fermi energy.

To assist in determining which compounds have the highest potential for application in solar cells, we have calculated the frequency-dependent absorption, $\alpha(\omega)$, of each compound, the results of which can be found in Fig. S9 of the ESI.† The major feature which we will focus on is the absorption onset, which represents the energy at which the absorption begins to rise substantially. For this work, we define the absorption onset to be the point at which the absorption coefficient reaches 10^3 cm^{-1}. The onset values are tabulated in Table 4. Our data matches well with both experimental data and previously calculated values for $CuTaN_2$, $CuNbN_2$, and $AgTaN_2$.[14,15,17] In order to be suitable for solar cells, a material should have a strong absorption onset in the range of 0.8–1.7 eV, and this onset should occur at a slightly higher energy than the band gap of that material.[17] Thus, based on the optical properties, five compounds potentially meet this criterion: $CuTaN_2$, $CuNbN_2$, $AgTaN_2$, $AgNbN_2$, and $AuNbN_2$. The absorption onsets of these five materials range from 0.88–1.75 eV.

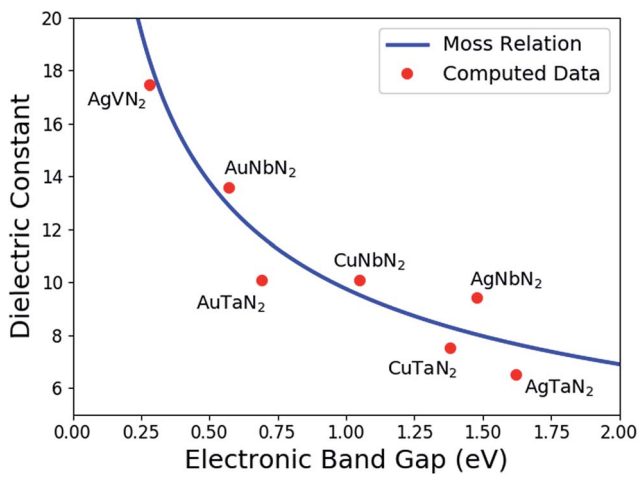

Fig. 4 Comparison between the computed data (red dots) of this work and the ideal Moss relation (blue solid line) for dielectric constants and band gaps. The dielectric constant is taken to be the arithmetic mean of the three directional components of ε_1 at zero frequency. Only data points for semiconductors are included in this plot, as the Moss relation does not apply to metallic compounds.

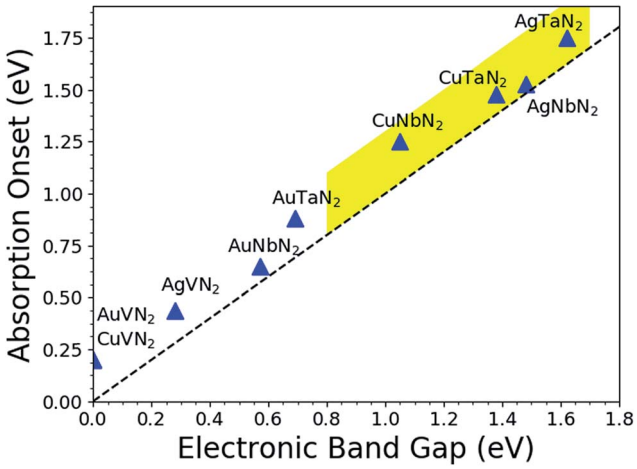

Fig. 5 Calculated absorption onset and electronic band gap of each compound. Materials which lie within the highlighted area are determined to be the most suitable compounds for solar energy conversion applications, according to the criterion discussed by A. Zakutayev *et al.*[14]

We have plotted the band gap *versus* absorption onset for each material in Fig. 5, to assist in visualizing and analyzing both the electronic and optical properties. In a similar manner to that of A. Zakutayev *et al.*,[14] we have highlighted the region which indicates the ideal optoelectronic properties for solar cell materials. Our findings show that four compounds fall within this region: $CuTaN_2$, $CuNbN_2$, $AgTaN_2$, and $AgNbN_2$. Therefore, these materials have the highest potential to be implemented in photovoltaics, and we suggest further experimental investigation would be beneficial in order to confirm this conclusion. We also find that $AuTaN_2$ and $AuNbN_2$ have properties which are near the ideal region, but each has a band gap and absorption onset which are slightly lower. However, these do have the possibility to be tuned by alloying with iso-electric substitutional atoms, which could make $AuTaN_2$ and $AuNbN_2$ solar cell material candidates as well.

4 Conclusion

In summary, we have investigated nine ternary nitrides of the form ABN_2, all of which exhibit the delafossite structure. Each

structure was geometrically optimized through standard *ab initio* techniques. Our computed lattice parameters match well with available experimental data for $CuTaN_2$, $CuNbN_2$, and $AgTaN_2$. For the remaining six compounds, we have provided a prediction for the structures. The in-plane lattice constant (a) is shown to be directly related to the B radius, while the out-of-plane lattice constant (c) is directly related to the A radius. To study the stability of these materials, we have computed formation energies, elastic constants, and phonon density of states. Formation energies and elastic moduli indicate all configurations to be energetically and mechanically stable. From analysis of phonon frequencies, we predict all compounds, except $AgVN_2$, to be stabilized at finite temperatures.

Hybrid functionals were implemented to study the electronic and optical properties of these delafossite nitrides. Electronic density of states display strong hybridization of the metal d electrons and the N p electrons, indicating strong covalent bonding, which is further supported by COHP analysis. Instabilities at 0 K can be attributed to significant A–N antibonding directly below the Fermi energy. In contrast, almost all compounds maintain substantial B–N bonding character throughout a wide range of occupied energies, thus signifying the importance of the B element in the stability of these compounds. The instability of $AgVN_2$ at higher temperatures is shown to be linked to strong A–N and B–N antibonding, which is a result of polyhedral distortions and enhanced localization of V d electrons. Calculated electronic band gaps match well with experimental data where it is available. Dielectric functions have been analyzed and the features explained in terms of d–d electronic transitions. The static dielectric constants and band gaps for the semiconductors agree very well with the Moss relation. Absorption onsets have been computed and the resulting data, along with the band gaps, indicate that $CuTaN_2$, $CuNbN_2$, $AgTaN_2$, and $AgNbN_2$ all have properties which make them suitable for application in solar energy conversion devices. $AuTaN_2$ and $AuNbN_2$ exhibit properties which, if tuned properly, could be useful as well.

Conflicts of interest

There are no conflicts of interest.

Acknowledgements

The computing for this project was performed at the Ohio Supercomputer Center (OSC).[68] We thank the National Science Foundation for funding this work through grants 1629230 and 1629239 under the CMMI and 1433467 under the EFRI-2DARE program. The authors also acknowledge funding support from the Air Force Research Laboratory, Space Vehicles Directorate, under Contract # FA9453-11-C-0253.

References

1 L. Suganthi and A. A. Samuel, *Renewable Sustainable Energy Rev.*, 2012, **16**, 1223–1240.
2 C. Wadia, A. P. Alivisatos and D. M. Kammen, *Environ. Sci. Technol.*, 2009, **43**, 2072–2077.
3 X. Wu, *Sol. Energy*, 2004, **77**, 803.
4 J. H. Scofield, A. Duda, D. Albin, B. L. Ballard and P. K. Predecki, *Thin Solid Films*, 1995, **260**, 26.
5 H. J. Snaith, *J. Phys. Chem. Lett.*, 2013, **4**, 3623.
6 H. Hoppe and N. S. Sariciftci, *J. Mater. Res.*, 2004, **19**, 1924.
7 B. K. Meyer, *et al.*, *Phys. Status Solidi B*, 2012, **249**, 1487–1509.
8 S. Rühle, *et al.*, *J. Phys. Chem. Lett.*, 2012, **3**, 3755–3764.
9 C. Kral, W. Lengauer, D. Rafaja and P. Ettymayer, *J. Alloys Compd.*, 1998, **265**, 215–233.
10 B. Eck, R. Dronskowski, M. Takahashi and S. Kikkawa, *J. Mater. Chem.*, 1999, **9**, 1527–1537.
11 P. G. Moses, M. Miao, Q. Yan and C. G. Van de Walle, *J. Chem. Phys.*, 2011, **134**, 084703.
12 A. Zakutayev, *J. Mater. Chem. A*, 2016, **4**, 6742–6754.
13 F. J. DiSalvo and S. J. Clarke, *Curr. Opin. Solid State Mater. Sci.*, 1996, **1**, 241–249.
14 A. Zakutayev, *et al.*, *Chem. Mater.*, 2014, **26**, 4970–4977.
15 M. Yang, *et al.*, *Energy Environ. Sci.*, 2013, **6**, 2994–2999.
16 U. Zachwieja and H. Jacobs, *Eur. J. Solid State Inorg. Chem.*, 1991, **28**, 1055–1062.
17 A. Miura, M. Wessel and R. Dronskowski, *J. Ceram. Soc. Jpn.*, 2011, **119**, 663–666.
18 D. B. Rogers, R. D. Shannon, C. T. Prewitt and J. L. Gillson, *Inorg. Chem.*, 1970, **10**, 723.
19 G. Kresse and J. Hafner, *Phys. Rev. B: Condens. Matter Mater. Phys.*, 1993, **47**, 558.
20 G. Kresse and J. Hafner, *Phys. Rev. B: Condens. Matter Mater. Phys.*, 1994, **49**, 14251.
21 G. Kresse and J. Furthmüller, *Comput. Mater. Sci.*, 1996, **6**, 15.
22 G. Kresse and J. Furthmüller, *Phys. Rev. B: Condens. Matter Mater. Phys.*, 1996, **54**, 11169.
23 P. E. Blöchl, *Phys. Rev. B: Condens. Matter Mater. Phys.*, 1994, **50**, 17953.
24 G. Kresse and D. Joubert, *Phys. Rev. B: Condens. Matter Mater. Phys.*, 1999, **59**, 1758.
25 A. Jain, S. P. Ong, *et al.*, *APL Mater.*, 2013, **1**, 011002.
26 X. Wu, D. Vanderbilt and D. R. Hamann, *Phys. Rev. B: Condens. Matter Mater. Phys.*, 2005, **72**, 035105.
27 F. Mouhat and F.-X. Coudert, *Phys. Rev. B: Condens. Matter Mater. Phys.*, 2014, **90**, 224104.
28 W. Voigt, *Lehrbuch der Kristallphysik*, B. G. Teubner, Verlag, Leipzig, 1928.
29 Y. Tian, B. Xu and Z. Zhao, *Int. J. Refract. Met. Hard Mater.*, 2012, **33**, 93.
30 B. Fultz, *Prog. Mater. Sci.*, 2010, **55**, 247.
31 O. Hellman, I. A. Abrikosov and S. I Simak, *Phys. Rev. B: Condens. Matter Mater. Phys.*, 2011, **84**, 180301.
32 O. Hellman and I. A. Abrikosov, *Phys. Rev. B: Condens. Matter Mater. Phys.*, 2013, **88**, 144301.
33 A. Togo and I. Tanaka, *Scr. Mater.*, 2015, **108**, 1.
34 Y. Wang, Z. T. Y. Liu, S. V. Khare, S. A. Collins, J. Zhang, L. Wang and Y. Zhao, *Appl. Phys. Lett.*, 2016, **108**, 061906.
35 S. Nosé, *Mol. Phys.*, 1984, **52**, 255.
36 J. Heyd, G. E. Scuseria and M. Ernzerhof, *J. Chem. Phys.*, 2006, **124**, 219906.

37 M. Gajdoŝ, K. Hummer, G. Kresse, J. Furthmuller and F. Bechstedt, *Phys. Rev. B: Condens. Matter Mater. Phys.*, 2006, **73**, 045112.
38 R. Deng, B. D. Ozsdolay, P. Y. Zheng, S. V. Khare and D. Gall, *Phys. Rev. B: Condens. Matter Mater. Phys.*, 2015, **91**, 045104.
39 E. Hecht, *Optics*, Addison-Wesley, Boston, 2002.
40 N. J. Szymanski, Z. T. Y. Liu, T. Alderson, N. J. Podraza, P. Sarin and S. V. Khare, *Comput. Mater. Sci.*, 2018, **146**, 310.
41 R. D. Shannon, *Acta Crystallogr.*, 1976, **32**, 751.
42 D. C. Gosh and R. Biswas, *Int. J. Mol. Sci.*, 2002, **3**, 87.
43 Z. T. Y. Liu, X. Zhou, D. Gall and S. V. Khare, *Comput. Mater. Sci.*, 2014, **84**, 365.
44 Z. T. Y. Liu, X. Zhou, S. V. Khare and D. Gall, *J. Phys.: Condens. Matter*, 2014, **26**, 025404.
45 Z. T. Y. Liu, D. Gall and S. V. Khare, *Phys. Rev. B*, 2014, **90**, 134102.
46 X. Zhou, D. Gall and S. V. Khare, *J. Alloys Compd.*, 2014, **595**, 80.
47 V. Adhikari, Z. T. Y. Liu, N. J. Szymanski, I. Khatri, D. Gall, P. Sarin and S. V. Khare, *J. Phys. Chem. Solids*, 2018, **120**, 197.
48 K. Balasubramanian, L. Huang and D. Gall, *Appl. Phys.*, 2017, **122**, 195101.
49 P. P. Gunaicha, S. Gangam, J. L. Roehl and S. V. Khare, *Sol. Energy*, 2014, **102**, 276.
50 J. A. Warner, S. K. R. Patil, S. V. Khare and K. C. Masiulaniec, *Appl. Phys. Lett.*, 2006, **88**, 101911.
51 V. Buršiková, P. Sládek, P. Sťahel and J. Buršík, *J. Non-Cryst. Solids*, 2006, **352**, 1242.
52 K. Balasubramanian, S. V. Khare and D. Gall, *Acta Mater.*, 2018, **152**, 175.
53 M. K. Singh, S. Dussan, G. L. Sharma and R. S. Katiyar, *J. Appl. Phys.*, 2008, **104**, 113503.
54 S. P. Pavunny, A. Kumar and R. S. Katiyar, *J. Appl. Phys.*, 2010, **107**, 013522.
55 N. P. Salke, K. Kamali, T. R. Ravindran, G. Balakrishnan and R. Rao, *Vib. Spectrosc.*, 2015, **81**, 112–118.
56 W. Shockley and H. J. Queisser, *J. Appl. Phys.*, 1961, **32**, 510.
57 R. Dronskowski and P. E. Blöchl, *J. Phys. Chem.*, 1993, **97**, 8617.
58 V. L. Deringer, A. L. Tchougreeff and R. Dronskowski, *J. Phys. Chem. A*, 2011, **115**, 5461.
59 S. Maintz, V. L. Deringer, A. L. Tchougreeff and R. Dronskowski, *J. Comput. Chem.*, 2013, **34**, 2557.
60 S. Maintz, V. L. Deringer, A. L. Tchougréeff and R. Dronskowski, *J. Comput. Chem.*, 2016, **37**, 1030.
61 S. Maintz, M. Esser and R. Dronskowski, *Acta Phys. Pol., B*, 2016, **47**, 1165.
62 M. Wuttig, D. Lüsebrink, D. Wamwangi, W. Wełnic, M. Gilleβen and R. Dronskowski, *Nat. Mater*, 2007, **6**, 122.
63 K. Burdett, R. Hoffmann and R. C. Fay, *Inorg. Chem.*, 1978, **17**, 2553.
64 M. E. Fleet, *Mineral. Mag.*, 1976, **40**, 531.
65 P. Kubáček and R. Hoffmann, *J. Am. Chem. Soc.*, 1981, **103**, 4320.
66 E. J. Little Jr and M. M. Jones, *J. Chem. Educ.*, 1960, **37**, 231.
67 T. S. Moss, *Photoconductivity in the elements*, Academic Press Inc., New York, 1952.
68 Ohio-Supercomputer-Center, 1987, https://osc.edu/ark:/19495/f5s1ph73.
69 K. Momma and F. Izumi, *J. Appl. Crystallogr.*, 2011, **44**, 1272.